

# The Incompatibility of Living Systems: Characterizing Growth-Induced Incompatibilities in Expanded Skin

ADRIAN BUGANZA TEPOLE,<sup>1</sup> MICHAEL GART,<sup>2</sup> CHAD A. PURNELL,<sup>2</sup> ARUN K. GOSAIN,<sup>2</sup> and ELLEN KUHL<sup>3</sup>

<sup>1</sup>Department of Mechanical Engineering, Stanford University, Stanford, CA 94305, USA; <sup>2</sup>Lurie Children's Hospital, Northwestern University Feinberg School of Medicine, Chicago, IL 60611, USA; and <sup>3</sup>Departments of Mechanical Engineering, Bioengineering, and Cardiothoracic Surgery, Stanford University, Stanford, CA 94305, USA

(Received 5 June 2015; accepted 22 September 2015)

Associate Editor Scott I. Simon oversaw the review of this article.

**Abstract**—Skin expansion is a common surgical technique to correct large cutaneous defects. Selecting a successful expansion protocol is solely based on the experience and personal preference of the operating surgeon. Skin expansion could be improved by predictive computational simulations. Towards this goal, we model skin expansion using the continuum framework of finite growth. This approach crucially relies on the concept of incompatible configurations. However, aside from the classical opening angle experiment, our current understanding of growth-induced incompatibilities remains rather vague. Here we visualize and characterize incompatibilities in living systems using skin expansion in a porcine model: We implanted and inflated two expanders, crescent, and spherical, and filled them to 225 cc throughout a period of 21 days. To quantify the residual strains developed during this period, we excised the expanded skin patches and subdivided them into smaller pieces. Skin growth averaged 1.17 times the original area for the spherical and 1.10 for the crescent expander, and displayed significant regional variations. When subdivided into smaller pieces, the grown skin patches retracted heterogeneously and confirmed the existence of incompatibilities. Understanding skin growth through mechanical stretch will allow surgeons to improve—and ultimately personalize—preoperative treatment planning in plastic and reconstructive surgery.

**Keywords**—Multi-view stereo, Isogeometric analysis, Skin, Incompatibility, Prestrain, Growth.

## INTRODUCTION

Common techniques in plastic and reconstructive surgery often lack quantitative understanding of the fundamental mechanisms that explain how tissues react to mechanical stimuli.<sup>30,67</sup> Even with a thorough

knowledge of the mechanobiology, personalizing treatment to an individual patient, a specific treatment modality, or a set of physiological conditions introduces an additional layer of complexity; planning the optimal procedure is virtually impossible by mere intuition.<sup>19</sup> Predictive computational simulations are an ideal tool for clinicians, linking basic material behavior and adaptation response to a clinical application in a patient specific case. Not surprisingly, new mechanical modeling and simulation paradigms are being constantly developed towards this goal.<sup>4</sup>

Tissue expansion is one prominent example of a popular medical procedure that requires knowledge of the fundamental adaptation processes of skin under extraordinary loading conditions, as well as a profound understanding of the clinical control variables: placement of the expander, timing of the inflation, shape of the expander, and geometries of the individual patient.<sup>12</sup> Despite its wide-spread use, tissue expansion still shows complications or suboptimal results in current clinical practice.<sup>25,36</sup> The execution of this technique relies heavily on the surgeon's experience.<sup>31</sup> However, recent computational approaches are beginning to address this need.<sup>15,50</sup>

Virtual tissue expansion in a personalized scenario is now within reach.<sup>69</sup> Using finite elements, we are able to represent complicated geometries encountered in the clinic and predict the acute and chronic tissue response.<sup>13,70</sup> The terms *acute* and *chronic* are used to distinguish deformations on the order of seconds to minutes, which are primarily elastic, from deformations on the order of days to weeks, which involve some degree of biological adaptation. The roadmap towards clinical acceptance of computational tools relies crucially on the experimental validation of these models. Numerous studies have looked at different markers of tissue

---

Address correspondence to Adrian Buganza Tepole, Stanford University, Stanford, CA, USA. Electronic mail: abuganza@stanford.edu

adaptation during tissue expansion using different animal models.<sup>5</sup> For example, it has been shown how at the end of the procedure, when the flap is harvested, skin typically retracts implying that not all the deformation is irreversible skin growth; skin expansion also induces some reversible elastic deformation.<sup>34</sup> Other groups have tested the mechanical properties of expanded skin at different time points and have showed that expanding skin *in vivo* leads to the deposition of new tissue which retains the same mechanical properties as the original, unexpanded skin.<sup>6,68</sup> More closely aligned with clinical outcomes, the quantification of net area gain has shown differences between different expander geometries and timing of inflations.<sup>44,65</sup>

Significant advancements have been made regarding the mechanotransduction pathways in stretched skin at the microscopic and molecular level. We now know that stretching beyond the physiological regime triggers enhanced cellular proliferation, collagen deposition, and revascularization.<sup>18,52,60</sup> This stretch is sensed by fibroblasts within the dermis to change their gene expression, which eventually results in the macroscopic effect of net tissue growth.<sup>66</sup>

However, despite tremendous progress, the numerous experiments around skin expansion and growth have mainly left out one key ingredient towards predictive medicine: a mathematical field theory capable of bridging the mechanics of tissue adaptation and the clinical loading scenario. We recently prototyped a novel experimental design motivated by the continuum mechanics of finite growth in living systems.<sup>10</sup> We use a well-established approach and introduce an intermediate incompatible configuration by splitting the deformation gradient into elastic and grown contributions.<sup>32</sup> When carried over to the experimental characterization of skin expansion, this conceptual approach is capable of revealing detailed regional variations of anisotropic skin stretch and growth.<sup>11</sup> Here we adopt this methodology to study the kinematics of skin expansion in a chronic porcine model using three basic ingredients: multi-view stereo, isogeometric description, and the continuum theory of finite growth.

Multi-view stereo is a technique we adopt from computer vision that allows the reconstruction of three-dimensional geometries out of a sequence of two-dimensional photographs.<sup>16</sup> The main advantages of multi-view stereo are its high accuracy and its versatility.<sup>58</sup> Unlike other experimental approaches such as binocular stereo, multi-view stereo does not require a restrictive setup with a controlled camera position; rather, its algorithm relies on a large amount of samples from a static scene and uses feature matching between pairs of photographs to calculate the calibration parameters of the camera.<sup>26</sup> Once the camera position and orientation are calibrated, an additional

optimization routine generates a dense three-dimensional point cloud of the scene.<sup>21</sup>

Isogeometric analysis is a computational approach to combine geometry and mechanical analysis. Once we have obtained the three-dimensional geometry from multi-view stereo, we need to represent it in such a way that is suitable for a continuum analysis. Traditionally, finite elements have been used to discretize the spatial domain and parameterize the fields of interest including the elastic strains and growth. Here we use B-splines surface patches to represent the geometry.<sup>51</sup> B-spline isogeometric analysis is currently gaining increasing attention.<sup>27</sup> Particularly, isogeometric analysis has been found suitable for thin shell descriptions of biological membranes such as skin.<sup>14</sup> Furthermore, a three-dimensional B-spline surface patch is defined explicitly over a two-dimensional parametric domain, inherently providing the same parameterization for every configuration of the tissue as it is expanded. Here we employ the isogeometric concept to retrieve the deformation maps and deformation gradients imposed by tissue expansion. At this point, our analysis is purely kinematic; yet, it lays the foundation to employ the same isogeometric description for predictive simulations of skin growth in response to expansion.

The continuum theory of finite growth serves to distinguish reversible, elastic deformations from irreversible, permanent growth. Following the classical theory, we introduce a reference configuration  $B_0$  and a deformed configuration  $B_t$  at time  $t$ . The map between the two is  $\varphi$  and its gradient  $F = \nabla_X \varphi$  is the key kinematic object that describes local changes. Figure 1 illustrates the multiplicative split of the deformation gradient into elastic contributions and growth,  $F = F^e \cdot F^g$ . This theory, originally proposed two decades ago,<sup>56</sup> has been widely used to mathematically characterize the adaptation of different tissues to mechanical cues.<sup>23</sup> The split of the deformation gradient

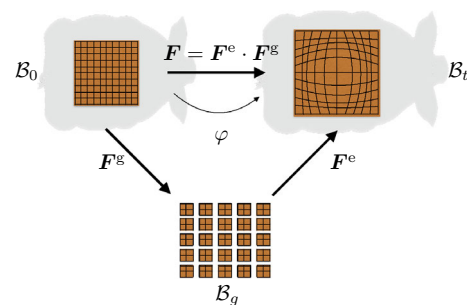


**FIGURE 1.** Finite growth is modeled mathematically using continuum mechanics. The reference configuration  $B_0$  is mapped to the deformed configuration  $B_t$  by  $\varphi$ . The gradient of this deformation,  $F$ , is split into an elastic contribution  $F^e$  and growth  $F^g$ . This introduces an incompatible intermediate configuration  $B_g$ .

introduces an intermediate incompatible configuration depicted in Fig. 1.<sup>40</sup> We can visualize this intermediate configuration by cutting the reference configuration into several small pieces, which are allowed to grow without constraints or applied forces according to the tensor field  $F^g$ . Clearly  $F^g$  defined in this fashion is not necessarily the gradient of a vector field, which is reflected through the notion of incompatibility. The elastic part of the deformation is indicated by  $F^e$  in Fig. 1. This field reflects the deformation required to patch the incompatibly grown parts together and apply the load. In other words,  $F^g$  captures the biology,  $F^e$  captures the loading and the residual stresses due to growth, and  $F$  captures the observed tissue deformation, which is a combination of elastic components and growth. Although this theoretical framework has become increasingly popular, the experimental characterization of the intermediate incompatible configuration attributed to growth does not seem to have been thoroughly studied except for very few special cases such as the well-known open angle experiment.<sup>22,35</sup>

We have previously quantified, for the first time, the detailed kinematics of an expansion procedure with rectangular tissue expander.<sup>10</sup> In clinical practice, however, expanders come in different sizes and shapes.<sup>55</sup> Figure 2 shows several commercial tissue expanders. Choosing one geometry over another is not a trivial task. Simulations and experiments have shown that different shapes produce different patterns of skin deformation and ultimately of skin growth.<sup>9,15</sup> Here we present the results of an experiment, which was designed as a natural follow up to our earlier publications.<sup>10,11</sup> The first novel contribution of the present study is the use of three expander geometries instead of one: spherical, rectangular, and crescent. For all three, we retain a strong interest in understanding the basic mechanisms of tissue adaptation with the ultimate goal of establishing a constitutive equation that links tissue stretch to growth over time. An important open question is associated with the notion of incompatibility induced by growth. The second major contribution of the present study is the quantification of residual deformations as a result of regional variations in the growth fields.

## MATERIALS AND METHODS

### *Animal Model*

Porcine models are a natural choice to study tissue expansion.<sup>5</sup> Experiments in pigs have improved our understanding of the histological and biomechanical changes of skin upon hyper-stretch.<sup>28</sup> The primary reason to choose a porcine expansion model is the similarity between the anatomical and mechanical

characteristics of human and young porcine integument.<sup>41–43</sup> From a clinical point of view, tissue expansion in the pig is similar to tissue expansion in humans, with similar criteria for expander selection, filling volume, and inflation timing.<sup>65</sup>

According to the protocol approved by the Ann & Robert H. Lurie Children's Hospital of Chicago Research Center Animal Care and Use Committee, we performed the experiment on a 1 month-old male Yucatan mini pig (Sinclair Biolabs, Columbus, MO). Previous expansion experiments on pigs have been done on both female and male specimens without distinction.<sup>7,9</sup> Furthermore, mechanical tests on human skin tissues have not pointed out significance differences attributed to gender.<sup>63</sup> Therefore we do not expect that there would be differences for our protocol if female pigs were used instead of male ones. We tattooed 10 cm × 10 cm grids with 1 cm line markings to the pig's skin using tattoo transfer medium in four areas: left caudal (P), right caudal (Q), left rostral (R), and right rostral (S), as illustrated in Fig. 3. We injected local anesthetic (1% lidocaine with 1:100000 epinephrine) subcutaneously at the site of each planned incision. We investigated three expanders geometries (PMT Corporation, Chanhassen, MN): spherical (P), rectangular (Q), and crescent (R), as illustrated in Fig. 2. Region S served as an internal control for prestrain and growth. We implanted the expanders subcutaneously, under the corresponding grids, and placed their filling ports near the dorsal midline, outside the measurement grids. We waited 14 days post-operatively to remove the sutures. We continued antibiotic prophylaxis for 48 h (Combi-Pen-48, Bimeda, Inc., Dublin, Ireland), and buprenorphine (0.05–0.1 mg/kg) for analgesia via intramuscular injection every 12 h for 4 doses, with additional doses available in case of animal distress.

We waited for the incisions to heal before beginning the expansion. We performed five inflation steps at 0, 2, 7, 10, and 15 days leading to filling volumes of 50, 75, 105, 165, and 225 cc. On day 21, we anesthetized the animal and recorded final measurements. We excised the four tattooed skin patches and euthanized the animal using intravenous overdose of pentobarbital (90 mg/kg). We took photographs of the explanted tissues. Finally, we performed a subdivision step and cut the original 11 × 11 grid into 5 × 5 smaller square pieces to further release residual stress. We fixed the tissues, and embedded them in paraffin for subsequent analyses. The present experiment was designed to prototype the method for a single animal. In the future, we will expand the study to multiple animals to explore multiple repeats of each expander geometry, different expander orientations with respect to Langer's lines,



**FIGURE 2.** Different tissue expander geometries are used in clinical practice. We are interested in comparing spherical expanders (top), rectangular expanders (middle), and crescent expanders (bottom).

and varying expander placements in the caudal and rostral regions.

#### *Kinematics Data Acquisition*

At every inflation step, we acquired 20 photographs of the experimental scene from different camera angles before and after filling. On the day of tissue harvest we photographed the final *in vivo* configuration, the excised *ex vivo* patches, and the subdivided pieces. We

reconstructed the three-dimensional surface geometry from the two-dimensional images using an online multi-view stereo service<sup>3</sup> (Autodesk Inc., San Rafael, California).

For calibration, we included two perpendicular rulers during the photo acquisition. The lengths of the rulers in the geometric reconstruction provide the scaling factors and allow us to quantify the relative error of the multi-view stereo algorithm. To scale each geometric model, we fitted a cubic spline to the

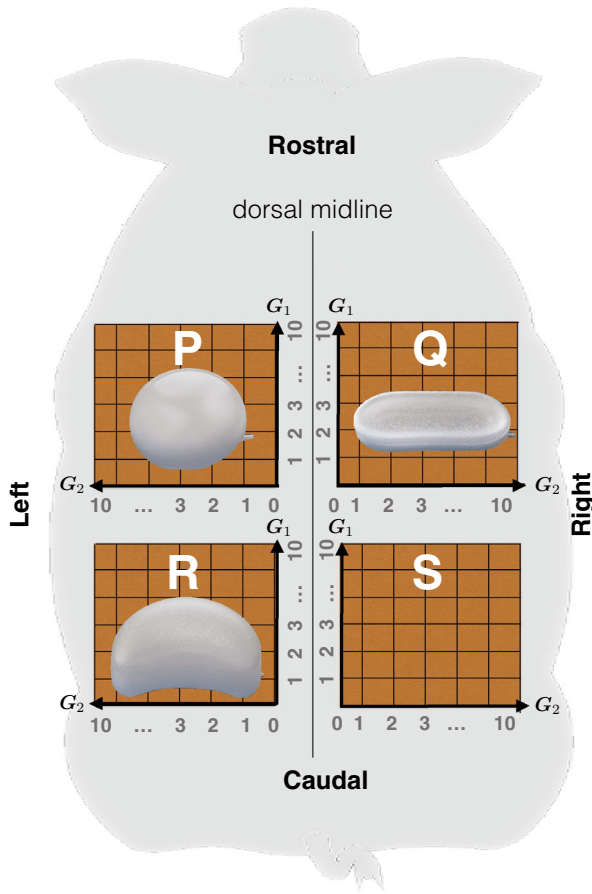


**FIGURE 3.** Porcine expansion model with four tattooed grids of  $11 \times 11$  points. A spherical expander is implanted underneath grid P, a rectangular expander underneath grid Q, and a crescent expander underneath grid R. Region S serves as control. Tangent vectors  $\mathbf{G}_1$  are aligned from caudal to rostral and vectors  $\mathbf{G}_2$  from midline to left and right.

reconstruction of the rulers and determined the individual lengths  $l_i$  along the spline between the  $i = 1, \dots, n$  1-cm-long ruler segments. We used the average length  $l = \sum_{i=1}^n l_i / n$  as scaling factor. The average error  $e = \sum_{i=1}^n e_i / n$ , calculated as the average of the individual reconstruction errors of each segment,  $e_i = [l_i - l] / l$ , served as a measure of algorithmic accuracy.

We created a B-spline surface patch for each grid by fitting the control points of the spline to best interpolate the  $11 \times 11$  tattooed nodes. A B-spline surface  $S(\xi, \eta)$  is the sum of a set of surface basis functions  $N_i(\xi, \eta)$  multiplied by the coordinates of a net of  $n_{cp}$  control points  $\mathbf{P}_i$ ,

$$S(\xi, \eta) = \sum_{i=0}^{n_{cp}} N_i(\xi, \eta) \mathbf{P}_i. \quad (1)$$

The surface basis functions  $N_i(\xi, \eta)$  are the tensor products of the B-spline basis functions  $N_i(\xi)$  and

$N_j(\eta)$ .<sup>51</sup> We parameterized the regions P, Q, R, and S at every time point with B-spline basis functions of polynomial degree  $p = 3$  based on knot vectors  $\Xi = \Theta = [0, 0, 0, 0, 1, 2, \dots, 9, 10, 10, 10, 10]$ . By fitting the same parameterization independently for all skin patches, we extracted the relative deformation between any two grids. For instance, choosing one of the B-spline surfaces as the reference state  $S_0$  and one as the deformed state  $S_t$ , we immediately recovered the referential and current coordinates over the same set of basis functions,

$$\mathbf{X} = \sum_{i=0}^{n_{cp}} N_i(\xi, \eta) \mathbf{P}_i \quad \text{and} \quad \mathbf{x} = \sum_{i=0}^{n_{cp}} N_i(\xi, \eta) \mathbf{p}_i, \quad (2)$$

The partial derivatives of the surface basis function with respect to the parametric coordinates define the covariant surface base vectors in the reference and deformed configurations,

$$\begin{aligned} \mathbf{G}_1 &= \sum_{i=0}^{n_{cp}} N_{i,\xi} \mathbf{P}_i & \mathbf{G}_2 &= \sum_{i=0}^{n_{cp}} N_{i,\eta} \mathbf{P}_i \\ \mathbf{g}_1 &= \sum_{i=0}^{n_{cp}} N_{i,\xi} \mathbf{p}_i & \mathbf{g}_2 &= \sum_{i=0}^{n_{cp}} N_{i,\eta} \mathbf{p}_i. \end{aligned} \quad (3)$$

The vectors  $\mathbf{G}_1$  and  $\mathbf{g}_1$  are aligned longitudinally, parallel to the long axis of the animal, while the vectors  $\mathbf{G}_2$  and  $\mathbf{g}_2$  are tangent to transverse coordinate lines. To determine the contravariant base vectors  $\mathbf{G}^\alpha$ , we calculated the covariant surface metric,

$$G_{\alpha\beta} = \mathbf{G}_\alpha \cdot \mathbf{G}_\beta \quad \text{with} \quad \alpha, \beta = 1, 2 \quad (4)$$

inverted it to calculate the contravariant surface metric  $G^{\alpha\beta}$ , and mapped the covariant base vectors  $\mathbf{G}_\beta$  onto their contravariant counterparts,

$$\mathbf{G}^\alpha = G^{\alpha\beta} \mathbf{G}_\beta \quad \text{with} \quad G^{\alpha\beta} = [G_{\alpha\beta}]^{-1}. \quad (5)$$

Finally, we calculated the deformation gradient  $\mathbf{F}$  as the dyadic product between the covariant deformed base vectors  $\mathbf{g}_\alpha$  and the contravariant reference base vectors  $\mathbf{G}^\alpha$ ,

$$\mathbf{F} = \mathbf{g}_\alpha \otimes \mathbf{G}^\alpha. \quad (6)$$

The deformation gradient is the key kinematic object to characterize the expansion process between any two time points across the tattooed grids. From it, we derived three measures of stretch: the area stretch  $\vartheta$  and the stretches  $\lambda_1$  and  $\lambda_2$  along the longitudinal and transverse directions. The area stretch captures the change in surface area between a surface element in the reference configuration  $S_0$  and in the deformed configuration  $S_t$ , and is the determinant of the deformation gradient,

$$\vartheta = \det(\mathbf{F}). \quad (7)$$

To characterize the anisotropy of the expansion processes, we used the right Cauchy Green deformation tensor  $\mathbf{C} = \mathbf{F}^T \cdot \mathbf{F}$  and calculated the stretches,

$$\lambda_1 = \sqrt{\mathbf{G}_1 \cdot \mathbf{C} \cdot \mathbf{G}_1} \quad \text{and} \quad \lambda_2 = \sqrt{\mathbf{G}_2 \cdot \mathbf{C} \cdot \mathbf{G}_2}, \quad (8)$$

along the longitudinal and transverse directions.

#### *Kinematic Analysis of Skin Expansion*

The deformation observed in the expanded patches is a combination of elastic components and growth. We built upon the usual split of the deformation gradient into two tensor fields,  $\mathbf{F} = \mathbf{F}^e \cdot \mathbf{F}^g$ . However, we refined this approach to account for prestrain and natural growth.<sup>11</sup> Figure 4 summarizes the important configurations during tissue expansion. The complete kinematic description of tissue adaptation under supra-physiological stretch required the analysis of both

the control and expanded patches. The control patch delivered information of prestrain and natural growth. The expanded patch captured the elastic deformation and growth. By combining these different measures of deformation, we calculated the amount of growth solely attributed to the expansion process.

The blue path in Fig. 4 refers to the kinematics of the control patch. While the expansion process took place, from day  $t = 0$  to day  $t = 21$ , the specimen grew naturally according to  $\mathbf{F}^{\text{gn}}$ . Skin, like most biological tissues, is not stress-free in its physiological state.<sup>2,54</sup> Furthermore, the morphological processes of growth and remodeling can lead to complex patterns of deformation and build-up of residual stresses.<sup>62</sup> The biological considerations that back up the multiplicative decomposition of the deformation gradient to include growth introduce a tensor field, which is not the gradient of a deformation and is thus incompatible.<sup>71</sup> We therefore quantified the amount of prestrain in two

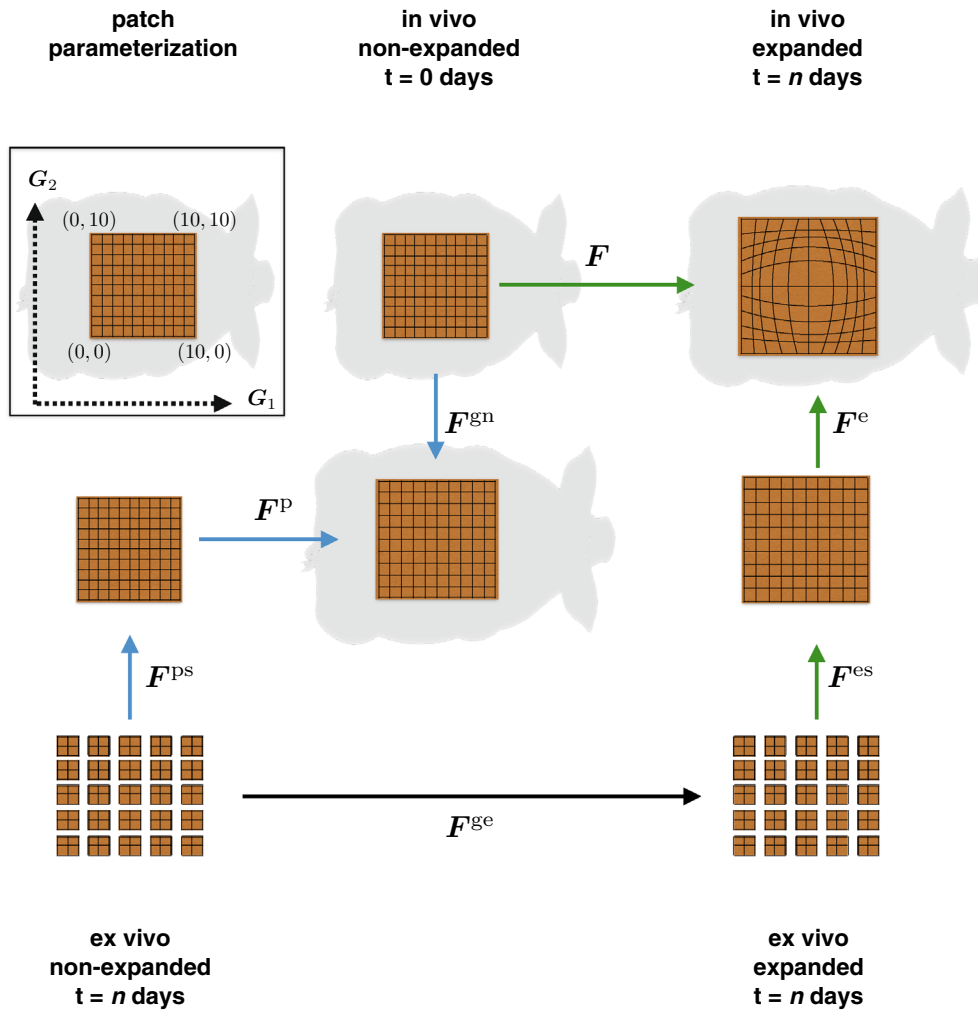


FIGURE 4. Configurations of skin expansion. In vivo, skin is subjected to prestrain,  $F^{\text{p}} \cdot F^{\text{ps}}$ . Expansion induces deformation,  $F$ . Excising the expanded patch releases the reversible, elastic deformation,  $F^{\text{e}} \cdot F^{\text{es}}$ . Skin growth,  $F^{\text{g}}$ , consists of natural growth,  $F^{\text{gn}}$ , and expansion-induced growth,  $F^{\text{ge}}$ .

steps. First, we studied the continuous deformation field that describes the retraction of an entire grid when harvesting the full-thickness skin patch, down to the fascia, from its *in vivo* environment. This field is described through the tensor  $\mathbf{F}^p$  in Fig. 4. Then, we subdivided the entire grid into  $5 \times 5$  smaller pieces and characterized the corresponding deformation  $\mathbf{F}^{ps}$ .

The green path in Fig. 4 refers to the kinematics of the expanded patches. The field  $\mathbf{F}$  describes the deformation at day  $t = n$  with respect to the *in vivo* state at day  $t = 0$ . At the end of the expansion process, not all of this deformation is irreversible skin growth, but some of it is elastic. By excising the patch and analyzing its retraction, we obtained a first approximation of the remaining elastic deformation at the end of an expansion procedure  $\mathbf{F}^e$ . Similarly to the control patches, the growth process described by the multiplicative decomposition of the deformation gradient alludes to an intermediate incompatible configuration and the existence of residual stresses. We further subdivided the *ex vivo* expanded patches into  $5 \times 5$  smaller pieces and calculated the incompatible field  $\mathbf{F}^{es}$ .

The black arrow in Fig. 4 refers to the kinematics of the growth attributed exclusively to the expansion process. Mathematically, we summarized Fig. 4 through the following composition of mappings,

$$\mathbf{F} \cdot \mathbf{F}^{gn-1} \cdot \mathbf{F}^p \cdot \mathbf{F}^{ps} = \mathbf{F}^e \cdot \mathbf{F}^{es} \cdot \mathbf{F}^{ge}. \quad (9)$$

Assuming that the prestrain of the control patches is the same throughout the expansion process we rearranged this mapping as follows,

$$\mathbf{F} \cdot \tilde{\mathbf{F}}^p \cdot \tilde{\mathbf{F}}^{ps} = \mathbf{F}^e \cdot \mathbf{F}^{es} \cdot \mathbf{F}^{ge} \cdot \mathbf{F}^{gn}, \quad (10)$$

where the pairs  $\{\mathbf{F}^p, \tilde{\mathbf{F}}^p\}$  and  $\{\mathbf{F}^{ps}, \tilde{\mathbf{F}}^{ps}\}$  differ only by a rigid body motion. In this setup, only the elastic deformation,  $\mathbf{F}^e \cdot \mathbf{F}^{es}$ , generates stress.<sup>53</sup> It is the combined analysis of the control and expanded patches

that allows us to isolate the amount of growth solely attributed to the expansion process:  $\mathbf{F}^{ge}$ . The control patches incorporate simple relaxation of the skin and realignment of collagen fibers in the absence of growth.

We postulate that skin grew only in the plane such that the thickness of an unloaded tissue sample remained constant throughout the growth process.<sup>70</sup> We allowed the in-plane area growth to be anisotropic with different growth factors longitudinally, along  $\mathbf{G}_1$ , and transversely, along  $\mathbf{G}_2$ ,<sup>23</sup> such that

$$\mathbf{F}^g = \mathbf{F}^{ge} \cdot \mathbf{F}^{gn} = \lambda_1^g \mathbf{G}_1 \otimes \mathbf{G}_1 + \lambda_2^g \mathbf{G}_2 \otimes \mathbf{G}_2 + \mathbf{N} \otimes \mathbf{N}. \quad (11)$$

This definition introduced a multiplicative split of the stretch measures. For the areal stretch, this implied that

$$\vartheta \vartheta^p \vartheta^{ps} = \vartheta^e \vartheta^{es} \vartheta^{ge} \vartheta^{gn}. \quad (12)$$

The specific assumption for the growth tensor introduced the total area growth as the product of the longitudinal and transverse stretches,  $\vartheta^g = \det(\mathbf{F}^g) = \lambda_1^g \lambda_2^g$ , with the anisotropic growth variables  $\lambda_1^g = \lambda_1^{gn} \lambda_1^{ge}$  and  $\lambda_2^g = \lambda_2^{gn} \lambda_2^{ge}$  also admitting a multiplicative split of the composed mappings  $\mathbf{F}^{ge}$  and  $\mathbf{F}^{gn}$ .

The deformation gradient  $\mathbf{F}$  was calculated with respect to the *in vivo* state at day  $t = 0$ . Hence, it captured the chronic deformation induced by the expansion process over the entire duration of the experiment. However, it is also of interest to determine the acute deformation.<sup>48,49</sup> It seems reasonable to assume that the acute deformation due to a single inflation step was mainly elastic. To calculate the acute deformation at the inflation step  $i$  we took the patch right before the inflation as the reference configuration and the patch immediately after the inflation as the deformed configuration. The gradient of this deformation  $\mathbf{F}_i^d$  neither

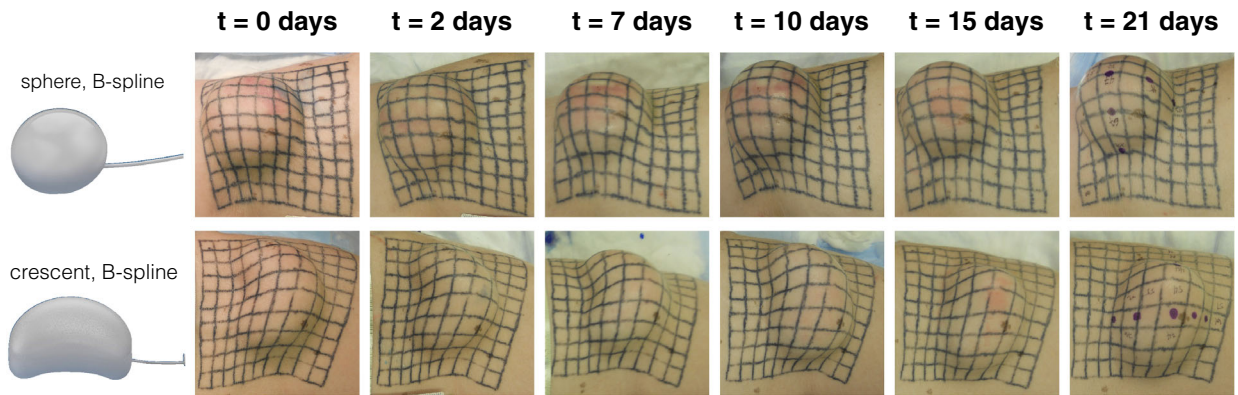


**FIGURE 5.** Sequence of inflation steps for a spherical and a crescent-shaped expander on a porcine model of tissue expansion. From left to right, each column depicts the five inflation steps at 0, 2, 7, 10, and 15 days leading to filling volumes of 50, 75, 105, 165, and 225 cc, respectively. The last column shows the expanded patches before excision at  $t = 21$  days.

affects the calculation of the chronic response nor of the final amount of skin growth.

## RESULTS

The expansion of the rectangular expander underneath grid Q failed due to device migration out of the reference grid. The expansion of the spherical and crescent expanders underneath grids P and R was successfully completed. Grid S was successfully explanted to serve as control. Figure 5 shows photographs of the grids P and R at the end of each inflation step. Both expanders were filled to the same volume at every time point. We performed five inflation steps at 0, 2, 7, 10, and 15 days to generate filling volumes of 50, 75, 105, 165, and 225 cc, respectively. On day 21, we euthanized the animal and harvested the skin patches. Table 1 summarizes the time points, volumes, and the reconstruction errors for grids P, R, and S.

Following the schematic in Fig. 4, we first present the results from the control patch S from which we calculated the natural growth tensor field,  $\mathbf{F}^{\text{gn}}$ , and the prestrain fields,  $\mathbf{F}^{\text{p}}$  and  $\mathbf{F}^{\text{ps}}$ . From the analysis of the expanded patches P and R, we extracted the deformation fields of the expansion-induced deformation,  $\mathbf{F}$ , and the fields of the elastic deformation revealed from the tissue harvest,  $\mathbf{F}^{\text{e}}$  and  $\mathbf{F}^{\text{es}}$  for the spherical and crescent expanders. The difference between expansion and control patches defined the expansion-induced growth,  $\mathbf{F}^{\text{eg}}$ , which we present last.

### Control Patches: Prestrain and Natural Growth

Patch S, which was not subjected to expansion, revealed the amount of natural growth and prestrain.

These deformation fields are illustrated in Fig. 4 by the blue path that connects the *in vivo* non-expanded state at day  $t = 0$  with the *ex vivo* subdivided patch at day  $t = 21$ .

Natural growth was isotropic and almost linear in time. Growth in each direction was of approximately 1% increase in length per day: In 21 days of natural growth, a unit square grew on average to a rectangle of dimensions  $1.19 \times 1.17$  yielding an average *in vivo* area gain of 1.38. Figure 6 illustrates the linear trend of natural growth in time. However, natural growth was not homogeneous. Table 2 highlights the regional variability in growth: Although the average area growth was 1.38, the maximum and minimum values were 1.90 and 0.92, respectively.

Excising the control grids at the end of the protocol revealed the first component of the prestrain,  $\mathbf{F}^{\text{p}}$ , which

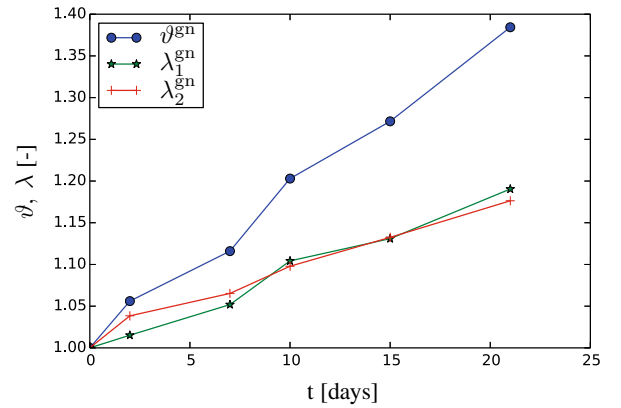


**FIGURE 6.** History of natural growth. Evolution of the naturally grown area  $v^{\text{gn}}$  and the naturally grown stretches  $\lambda_1^{\text{gn}}$  and  $\lambda_2^{\text{gn}}$ . Natural growth is isotropic and almost linear with directional growth of approximately 1% per day. During 21 days, a unit square grows to a rectangle of dimensions  $1.19 \times 1.17$  with an average area gain of 1.38.

**TABLE 1.** Summary of the expansion protocol with spherical expander on patch P, crescent expander on patch R, and control patch S.

Patch	$t = 0$		$t = 2$		$t = 7$		$t = 10$		$t = 15$		$t = 21$		
	Pre	Post	Pre	Post	Pre	Post	Pre	Post	Pre	Post	Pre	<i>Ex-vivo</i>	Subdivided
P													
V (cc)	0	50	50	75	75	105	105	165	165	225	225	–	–
Error (%)	1.5	1.2	1.5	2.0	1.3	1.4	1.3	1.1	1.0	1.2	1.5	1.8	1.0
R													
V (cc)	0	50	50	75	75	105	105	165	165	225	225	–	–
Error (%)	1.5	1.2	1.5	2.0	1.3	1.4	1.3	1.1	1.0	1.2	1.5	0.8	0.8
S													
V (cc)	0	0	0	0	0	0	0	0	0	0	0	–	–
Error (%)	1.0	1.5	1.6	1.6	1.1	2.0	0.5	1.4	1.0	1.5	0.9	1.6	1.1

The rectangular expander on patch Q migrated out of the reference grid. The final filling volume at the end of the protocol at day  $t = 21$  was 225 cc. We reconstructed the geometry of every grid, at every time point, before and after expansion. On day  $t = 21$  we reconstructed the *in vivo* patch, the *ex vivo* excised patch, and the subdivided excised patch.

was a continuous field. To illustrate that remaining residual stresses exist, we further subdivided the excised control patch into  $5 \times 5$  smaller pieces, which defined the discontinuous field,  $F^{ps}$ .<sup>1</sup>

Figure 7 illustrates the spatial distribution of the total prestrain. The prestrain field was neither homogeneous nor continuous: The subdivision step revealed the discontinuity of the deformation map. The prestrain measures plotted in Fig. 7 were continuous within each one of the smaller patches, but discontinuous across the patch boundaries. This illustrates the incompatible configuration associated with the continuum theory of finite growth.

The first component of the prestrain,  $F^P$ , shows that a unit square *in vivo* retracted on average to a square with a side length of 0.89. The subdivision step led to further shrinkage and the emergence of anisotropy. In combination, the excision and subdivision of the control patches show that on average skin was prestrained by 1.14 in the direction of the long axis of the pig and by 1.19 in the transverse direction, see Table 3.

#### Expanded Patches: Expansion-Induced Deformation and Elastic Deformation

Patches *P* and *R* provided information related to the expansion-induced deformation and the final elastic deformation. The maps describing these relations are shown with the arrows colored in green in Fig. 4. By taking the pig at day  $t = 0$  as reference configuration,

**TABLE 2. Summary of growth  $F^{gn}$  from analyzing patch S between the non-expanded states at days  $t = 0$  and  $t = 21$ .**

Deformation	Max	Min	Avg
$\vartheta^{gn} (-)$	1.90	0.92	1.38
$\lambda_1^{gn} (-)$	1.39	0.91	1.17
$\lambda_2^{gn} (-)$	1.51	0.87	1.19

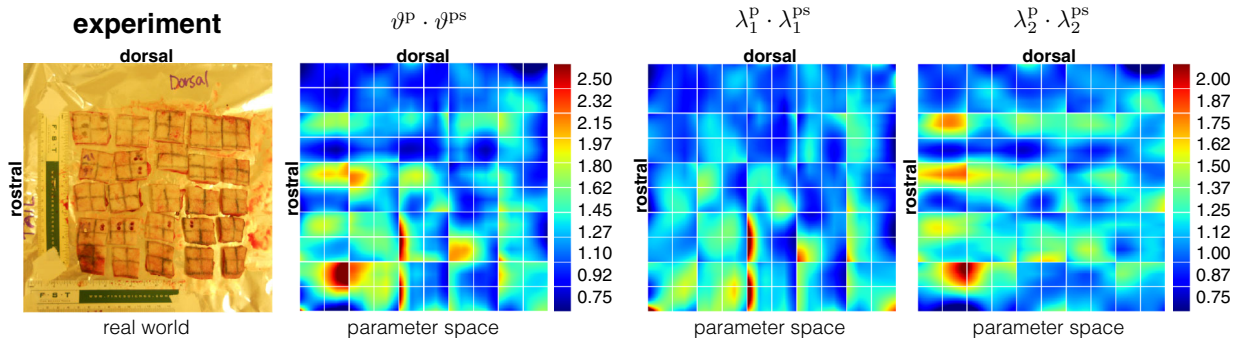
we quantified the deformation induced throughout the expansion process. The gradient of this deformation map was used to characterize the local changes in geometry.

Figure 8 shows the contour plots of the spatial distribution of the chronic deformation for patches *P* and *R* of the spherical and crescent expanders. We use the term *chronic* deformation because at every time point we are interested in the map with respect to the reference pig at day  $t = 0$ . Table 4 summarizes our findings. The expansion process spanned  $t = 21$  days with inflations at days  $t = 0, 2, 7, 10, 15$ . At the end of  $t = 21$  days the spherical and crescent expanders were filled to a final volume of 225 cc. The spherical expander deformed a unit square into a rectangle of dimensions  $1.33 \times 1.27$ . The crescent expander deformed a unit square into a rectangle of dimensions  $1.25 \times 1.20$ . In both cases the longitudinal direction deformed more than the transverse direction.

We also quantified the deformation that occurred during each inflation step, which we refer to as *acute*, and plot the corresponding stretch contours in Fig. 9. Each contour plot illustrates the measures of strain with the patch right before the inflation as reference configuration and the patch immediately after the

**TABLE 3. Summary of prestrain  $F^P$  and  $F^{ps}$  from analyzing patch S upon excision and further subdivision.**

Deformation	Max	Min	avg
$\vartheta^P (-)$	2.12	0.66	1.24
$\lambda_1^P (-)$	1.60	0.70	1.12
$\lambda_2^P (-)$	1.63	0.75	1.12
$\vartheta^{ps} (-)$	2.00	0.65	1.05
$\lambda_1^{ps} (-)$	1.81	0.70	1.00
$\lambda_2^{ps} (-)$	1.49	0.75	1.04
$\vartheta^P \cdot \vartheta^{ps} (-)$	1.90	0.92	1.38
$\lambda_1^P \cdot \lambda_1^{ps} (-)$	2.33	0.77	1.14
$\lambda_2^P \cdot \lambda_2^{ps} (-)$	2.10	0.79	1.19



**FIGURE 7. Prestrain upon excision and further subdivision of the control patch S. Skin releases the elastic stresses upon excision and subdivision, left. The prestrain field is a composition of the excision and subdivision maps  $F^P$  and  $F^{ps}$ . The resulting configuration is incompatible. The contour maps highlight the incompatibility of the total area prestretch and the prestretch in longitudinal and transverse directions.**

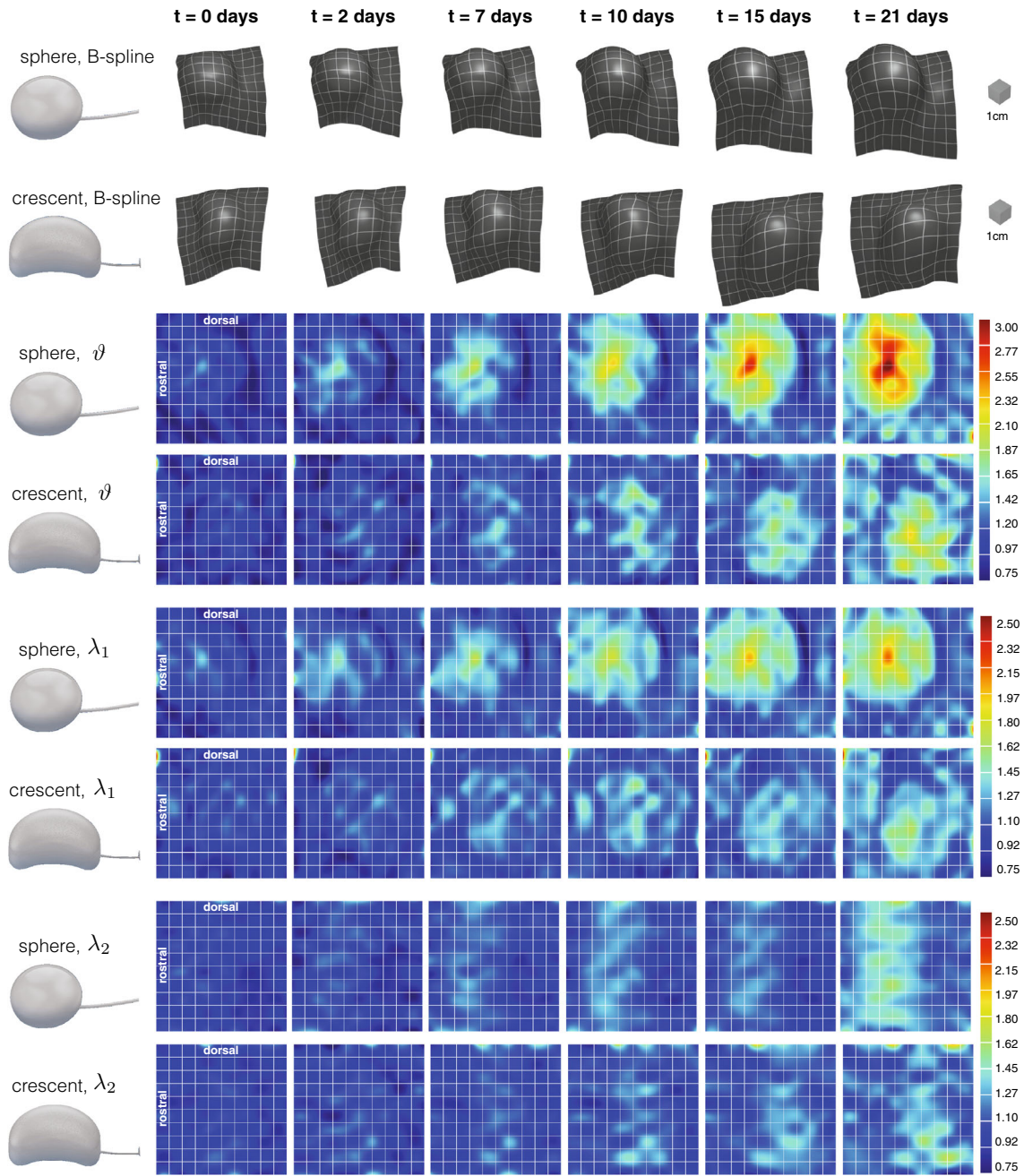


**FIGURE 8.** Chronic deformation induced by tissue expansion. The columns depict the chronic overstretch due to a sequence of inflations at the given time points. The first two rows show the total area change  $\vartheta$  for the spherical and crescent expanders in the patches P and R. The middle and bottom rows show the corresponding stretches  $\lambda_1$  and  $\lambda_2$  aligned with and perpendicular to the long axis of the pig. Deformations along the long axis are greater than those perpendicular to the long axis. Deformations induced by the spherical expander are larger than those by the crescent expander even though both devices were filled to the same volume.

inflation as deformed configuration. This setup defined the deformation gradient  $F_i^d$  for each inflation  $i$ .

The values of the acute strains across the different inflation steps remained fairly similar and close to one as seen in Table 5. There was, however, a marked regional variation of the strain contours: The total area

stretch and the longitudinal stretch exhibited larger values towards the central area of the expander and compressive stretches in the periphery of the expanded regions. The transverse stretch did not follow this trend. We remark though that this acute deformation did not enter the calculation of the final growth. As

**TABLE 4.** Chronic deformation history  $F$  from analyzing patches  $P$  and  $R$  during tissue expansion between days  $t = 0$  and  $t = 21$ .

$t$ (days)	Expander (-)	Volume (cc)	$\vartheta$ (-)			$\lambda_1$ (-)			$\lambda_2$ (-)		
			Max	Min	Avg	Max	Min	Avg	Max	Min	Avg
0	Sphere	50	1.44	0.71	0.98	1.37	0.76	1.00	1.17	0.84	0.97
0	Crescent	50	1.46	0.76	0.98	1.24	0.79	1.00	1.17	0.84	0.98
2	Sphere	75	1.74	0.68	1.08	1.51	0.73	1.08	1.19	0.75	1.00
2	Crescent	75	1.43	0.66	1.00	1.31	0.65	1.00	1.26	0.77	1.00
7	Sphere	105	2.01	0.69	1.21	1.70	0.75	1.13	1.32	0.84	1.07
7	Crescent	105	1.66	0.83	1.15	1.40	0.87	1.11	1.33	0.86	1.03
10	Sphere	165	2.26	0.74	1.36	1.76	0.77	1.21	1.39	0.83	1.11
10	Crescent	165	1.86	0.87	1.26	1.58	0.80	1.15	1.45	0.83	1.09
15	Sphere	225	2.77	0.72	1.52	2.01	0.69	1.29	1.47	0.89	1.18
15	Crescent	225	1.87	0.83	1.32	1.46	0.84	1.17	1.44	0.92	1.14
21	Sphere	225	3.09	0.93	1.70	2.13	0.90	1.33	1.62	0.98	1.27
21	Crescent	225	2.25	0.87	1.49	1.66	0.85	1.25	1.67	0.96	1.20

summarized in Eq. (10), the growth calculations were based exclusively on the *chronic* deformation  $F$ .

Figure 10 summarizes the elastic deformation released upon excision and further subdivision of the expanded patches P and R. Upon excision, the expanded patches retracted revealing that not all the deformation imposed by the expansion process is attributed to growth. This retraction was the elastic deformation  $F^c$  of the total deformation at the end of the experimental protocol. The first component of the elastic deformation captured in the field  $F^c$  was continuous. However, we anticipated that the excised patch was not stress-free. The biological description of growth as a local deposition of new material suggested the subdivision of the patch into smaller pieces to further relieve residual stresses. Figure 10 left depicts photographs of the experimental setup in which the excised patches P and R were subdivided into  $5 \times 5$  pieces. The resulting tensor  $F^{es}$  captured the incompatibility between the excised and subdivided patches. The composition of both tensors yielded the total elastic deformation  $F^c \cdot F^{es}$ . The contour maps of Fig. 10 summarize the area, longitudinal and transverse stretches, of this composed map for the spherical and crescent expanders.

On average, the elastic deformation was slightly larger in the transverse direction than in the longitudinal direction, as synthesized in Table 6. The spherical expander induced a larger elastic retraction than the crescent expander. On average, a unit square from patch P retracted to a rectangle of dimensions  $0.87 \times 0.82$  while a unit square from patch R shrank into a  $0.88 \times 0.87$  rectangle. There was significant regional variation in both cases, the total area stretch as well as the longitudinal stretch reflected the placement of the expander, while the transverse stretch was slightly more homogeneous.

#### Control Patches Vs. Expanded Patches: Expansion-Induced Skin Growth

By combining the information from the control patches and the expanded patches we were able to quantify the amount of growth caused by the expansion process alone. Figure 4 indicates the mappings associated with the control patches through blue arrows and with the expanded patches through green arrows. The black arrow connecting the subdivided *ex vivo* control patch and the subdivided *ex vivo* expanded patch is the deformation that characterizes expansion-induced growth. At this point, we have presented the fields  $F^p \cdot F^p$  and  $F^{en}$  from the control patch. The fields  $F^c \cdot F^{es}$  and  $F$  were obtained from the analysis of patches P and R. We could then calculate the expansion induced growth  $F^{ge}$  from Eq. (10).

The total area growth averaged 1.17 for the spherical and 1.10 for the crescent expander, see Table 7. Growth was anisotropic with larger longitudinal than transverse growth. On average, a unit square from patch P grew into a rectangle of dimensions  $1.11 \times 1.05$ , a unit square on patch R became a rectangle of  $1.08 \times 1.02$ .

Figure 11 shows the contour plots of the growth measures for the spherical and crescent expanders. The spherical expander triggered a growth pattern that reflects the placement of the expander. The crescent expander triggered larger growth in the regions above the expander towards the end of the expansion process; however, it also triggered growth in remote regions.

## DISCUSSION

This manuscript presents the kinematic characterization of a skin expansion procedure on a porcine

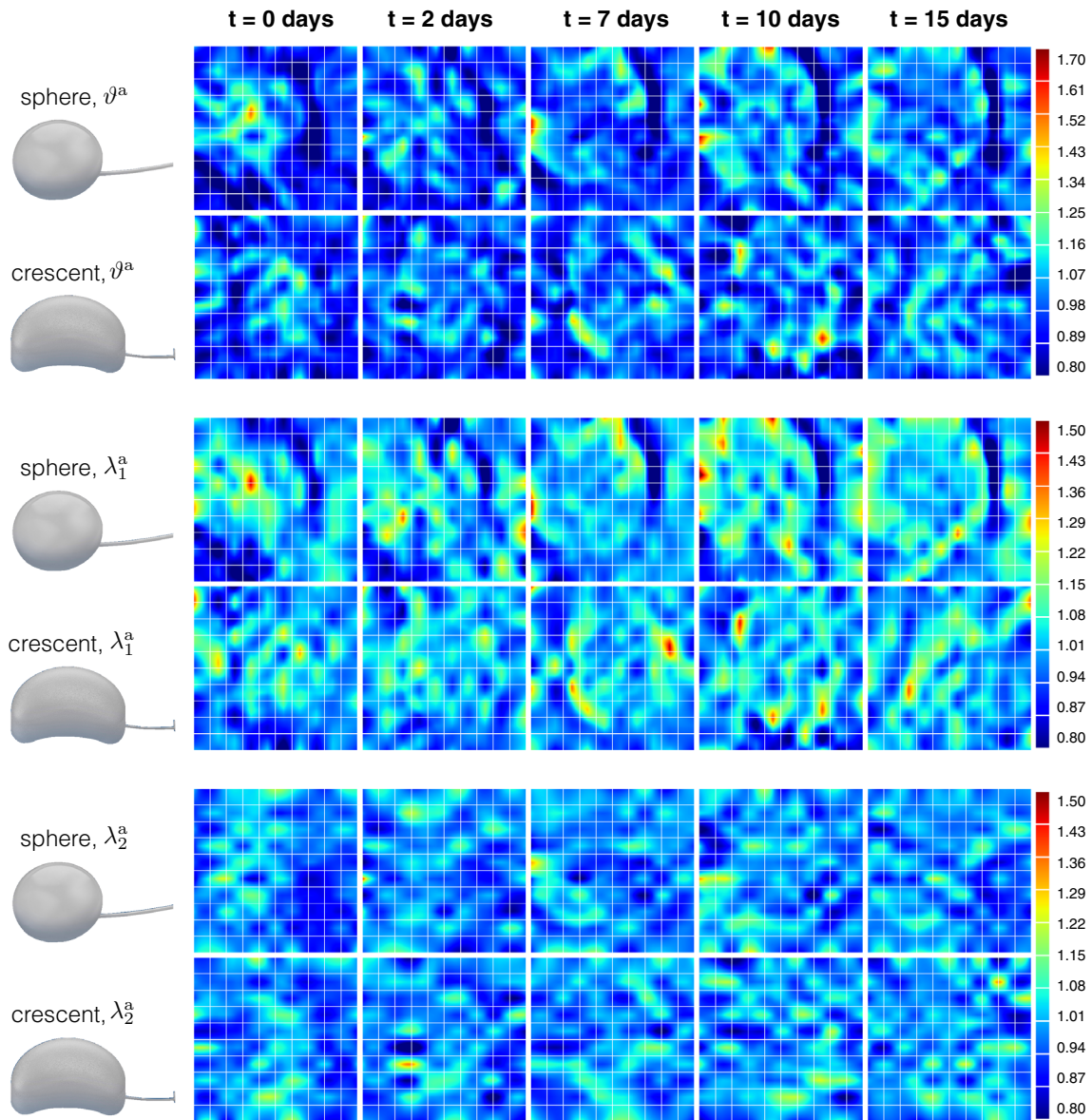


**FIGURE 9.** Acute deformation induced by tissue expansion. The columns depict the acute deformation imposed by a single inflation step at different time points. The first two rows show the acute area change  $\vartheta^a$  for the spherical and crescent expanders in the patches P and R. The middle and bottom rows show the corresponding acute stretches  $\lambda_1^a$  and  $\lambda_2^a$  aligned with and perpendicular to the long axis of the pig. Deformations along the long axis are greater than those perpendicular to the long axis. Deformations induced by the spherical expander are larger than those by the crescent expander even though both devices were filled to the same volume at each inflation step.

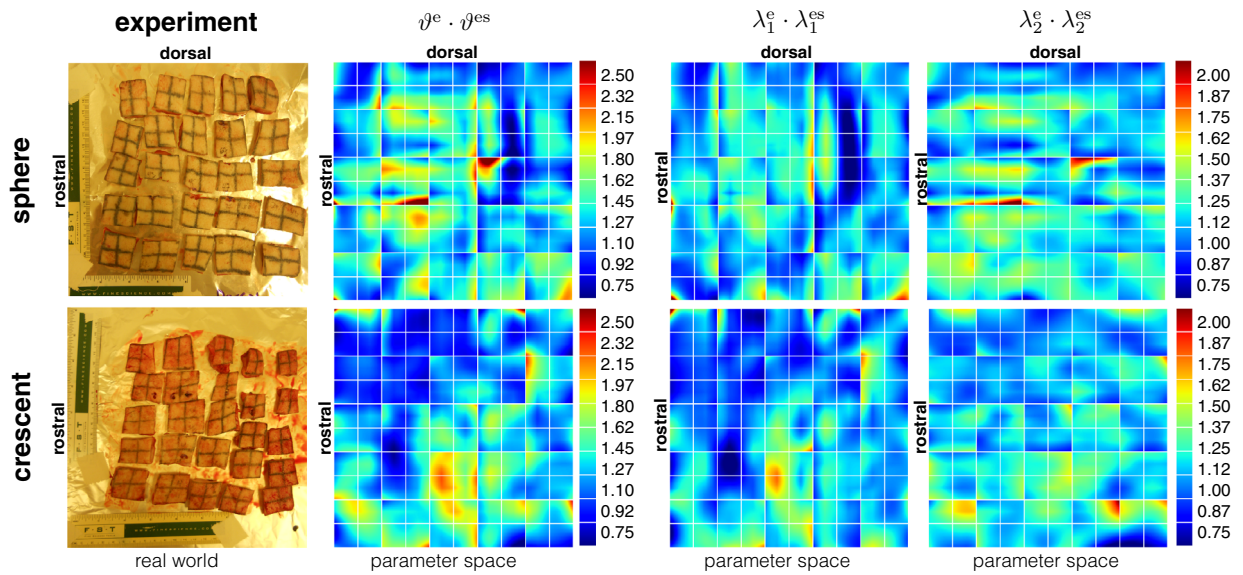
model using multi-view stereo, isogeometric analysis, and the continuum theory of finite growth. The present work builds upon a methodology recently introduced by our group.<sup>10</sup> Our first experiment reported growth induced by a rectangular expander and it served as a proof of concept. Here we aimed at comparing three different expander geometries: spherical, rectangular and crescent. Unfortunately, the rectangular expander migrated out of the reference grid and we disregarded its analysis. For all other patches, we not only com-

pared the growth itself, but also characterized the incompatibility of living systems.

The core of the theory of finite growth is the notion of an incompatible grown configuration.<sup>32</sup> The deformation gradient is split into elastic contributions and growth,  $\mathbf{F} = \mathbf{F}^e \cdot \mathbf{F}^g$ . The tensor field  $\mathbf{F}^g$  reflects the biological response, it captures mathematically how tissues respond to mechanical cues. This field is not the gradient of a deformation, which implies that it introduces incompatibility. To quantify incompatibil-

**TABLE 5. Acute deformation history  $F^a$  from analyzing patches  $P$  and  $R$  during tissue expansion at days  $t = 0$  to  $t = 15$ .**

$t$ (days)	Expander (-)	Volume (cc)	$\vartheta^a$ (-)			$\lambda_1^a$ (-)			$\lambda_2^a$ (-)		
			Max	Min	Avg	Max	Min	Avg	Max	Min	Avg
0	Sphere	50	1.32	0.72	0.98	1.44	0.75	1.00	1.23	0.83	0.97
0	Crescent	50	1.50	0.71	0.98	1.30	0.80	1.00	1.21	0.84	0.98
2	Sphere	75	1.36	0.69	0.98	1.26	0.66	1.00	1.20	0.80	0.98
2	Crescent	75	1.31	0.61	0.98	1.24	0.80	1.01	1.34	0.68	0.97
7	Sphere	105	1.40	0.79	0.98	1.30	0.57	1.00	1.20	0.77	0.98
7	Crescent	105	1.37	0.59	1.00	1.46	0.83	1.02	1.16	0.77	0.98
10	Sphere	165	1.60	0.73	1.01	1.35	0.60	1.02	1.25	0.75	0.99
10	Crescent	165	1.48	0.58	1.01	1.42	0.75	1.02	1.22	0.77	1.00
15	Sphere	225	1.27	0.73	1.01	1.35	0.55	1.02	1.22	0.79	0.98
15	Crescent	225	1.34	0.54	1.02	1.37	0.80	1.02	1.32	0.81	1.00


**FIGURE 10. Elastic deformation released upon excision and further subdivision of the expanded patches  $P$  and  $R$ . Skin releases the elastic stress upon excision and subdivision, left. The total elastic deformation is a composition of excision and subdivision maps  $F^e$  and  $F^{es}$ . The resulting configurations are incompatible. The contour maps highlight the incompatibility of the total elastic area deformation and the elastic stretch in longitudinal and transverse directions.**

ity experimentally, we subdivide the excised grown skin patches into  $5 \times 5$  smaller pieces and calculate the corresponding deformation fields. While incompatibility has been characterized in tubular tissues through the global measure of the opening angle,<sup>22</sup> this study is the first to quantify incompatibility for an entire field quantity.

We characterize the kinematics of skin expansion through three modular analyses: The kinematics of the control patch provides information about natural growth and tissue prestrain. The kinematics of the expanded patches provide information about the deformation induced by the device and the elastic deformation released upon excision. The combination

of these two analyses defines the growth attributed to the expansion process alone.

Natural growth during  $t = 21$  days revealed that the specimen grows at a nearly linear rate and reaches a value of  $\vartheta^{en} = 1.38$ . This is consistent with our previous experiments in which the specimen grew a total of 1.48 times in area in  $t = 37$  days. The natural growth rate for our previous experiment was 0.04/day, here it is 0.06/day. While this reveals the importance of variation between animals, these values are still within the same order of magnitude.

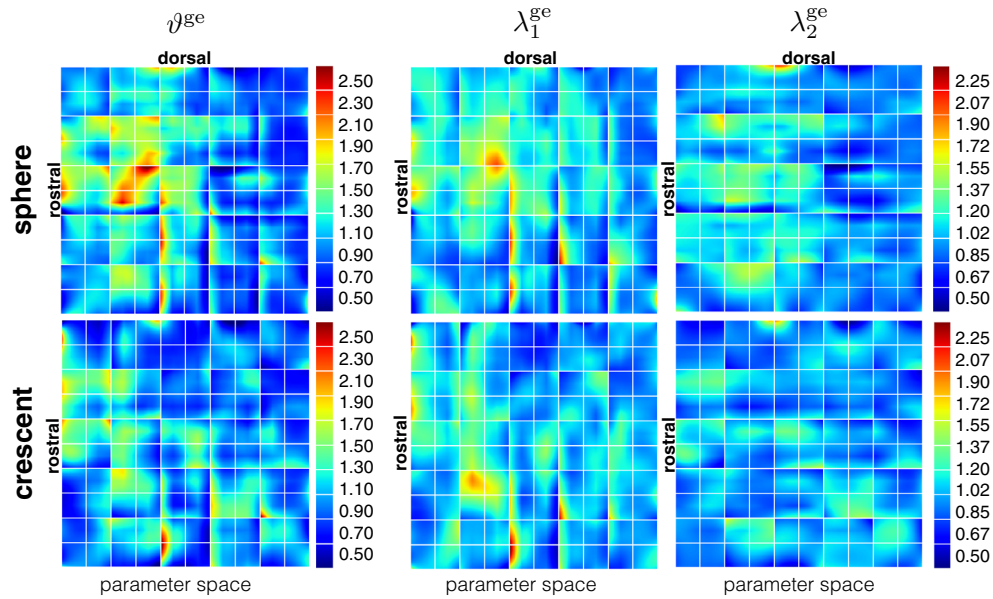
Prestrain agrees well with our previous results. Once more, we find the importance of inter-animal variation. While previously we reported an isotropic area pre-

**TABLE 6.** Summary of elastic deformation  $F^e$  and  $F^{es}$  from analyzing the excised patches P and R corresponding to the spherical and crescent expanders.

Deformation	Sphere			Crescent		
	Max	Min	Avg	Max	Min	Avg
$\vartheta^e (-)$	2.55	0.73	1.42	1.98	0.77	1.27
$\lambda_1^e (-)$	1.71	0.75	1.19	1.50	0.69	1.13
$\lambda_2^e (-)$	1.90	0.90	1.21	1.65	0.88	1.14
$\vartheta^{es} (-)$	1.93	0.46	0.97	1.89	0.69	1.02
$\lambda_1^{es} (-)$	1.56	0.67	0.96	1.55	0.69	0.98
$\lambda_2^{es} (-)$	1.89	0.56	1.00	1.79	0.74	1.03
$\vartheta^e \cdot \vartheta^{es} (-)$	3.40	0.60	1.39	2.29	0.74	1.32
$\lambda_1^e \cdot \lambda_1^{es} (-)$	1.85	0.63	1.15	1.83	0.66	1.12
$\lambda_2^e \cdot \lambda_2^{es} (-)$	2.38	0.83	1.22	2.11	0.87	1.18

**TABLE 7.** Summary of expansion-induced growth  $F^{ge}$  from combining the analysis of the excised patches P and R corresponding to the spherical and crescent expanders with the analysis of the control patch S.

Deformation	Sphere			Crescent		
	Max	Min	Avg	Max	Min	Avg
$\vartheta^{ge} (-)$	2.65	0.43	1.17	2.53	0.55	1.10
$\lambda_1^{ge} (-)$	2.13	0.47	1.11	2.26	0.57	1.08
$\lambda_2^{ge} (-)$	1.79	0.45	1.05	1.68	0.59	1.02

**FIGURE 11.** Growth induced by the expansion process. The spherical expander, top, induces a larger amount of growth compared to the crescent expander, bottom. The contour maps highlight area growth and the growth in the longitudinal and transverse directions.

strain prior to subdivision of 1.44, here the corresponding average is 1.24. We consistently observed that prestretch is isotropic although the tissue itself is highly anisotropic.<sup>57,64</sup> In our previous experiment, the reconstruction error for the excised control patch was 10%, significantly larger than here with 2% and less.

Here, after excising the entire grid, we further release residual stress by subdividing the patch into smaller pieces. The resulting deformation field becomes discontinuous across the patch boundaries. Naturally, this additional subdivision step alters the total pre-strain and reveals anisotropy, which had been unde-

tected when considering the full patch. We now define the total prestrain as the composition of excision and subdivision. With the subdivision included, the total prestrain averages 1.38, an increase of 11.3% as compared to excision alone. When the full, intact patch is considered, both longitudinal and transverse directions show stretches of 1.12. Upon subdivision, the transverse direction shows a higher total prestretch of 1.19 compared to 1.14 in the longitudinal direction. This suggests that the incompatibility of living systems plays an important role in the *in vivo* setting.

The *in vivo* deformation and the elastic deformation upon excision differ significantly for different expander geometries. In clinical practice, expanders come in different sizes and shapes. Simulations and experiments have shown that varying the expander geometry alters the resulting deformation field and, consequently, the regional variation of skin growth.<sup>9,15</sup> Choosing the *in vivo* state at day  $t = 0$  as reference configuration, allows us to characterize the *chronic* tissue response. As we had previously predicted computationally,<sup>15</sup> even though both expanders were filled to the same volume of 225 cc, the spherical device induces an average area change of 1.70 at  $t = 21$  days while the crescent expander results in an area change of 1.49. In our previous experiment we determined an area change of 1.73 at  $t = 20$  days for a filling volume of 200cc for the rectangular expander. In agreement with our computational predictions, both spherical and rectangular expanders induce larger deformations than the crescent device. The comparison with the rectangular expander from the previous experiment has to be done with caution though since the inflation protocol was not exactly the same as the one followed here. The deformation induced by the devices is anisotropic and displays the same trend for both expander geometries: longitudinal stretches are always larger than transverse stretches. This finding is also consistent with our initial experiment, and suggests that anisotropic material properties of porcine skin are significant and more important than the shape of the expander.<sup>29</sup>

In addition to the *chronic* response, we also characterize the *acute* response by choosing the patch right before the inflation as reference configuration and the patch immediately after inflation as deformed configuration. The average values for the strains are surprising. On average, the area change over the grid is close to one. In fact, the average longitudinal stretches are always tensile,  $\lambda_1^a \geq 1.0$ , and the average transverse stretches are always compressive,  $\lambda_2^a \leq 1.0$ . This seems counterintuitive, since we would expect that each inflation step imposes stretches larger than one. Looking closer at the regional stretch variation, we do

find this to be the case: the contour maps for  $\lambda_1^a$  reflect the placement of the expander, with values in the range 1.00 to 1.50. The contours of  $\lambda_2^a$  seem to capture the region along the longitudinal axis in which the expander is placed, but they do not show great variation along the transverse axis. It seems reasonable to assume that the acute response is dominated by the elastic properties of the tissue and not by growth. Coherent with this assumption, the acute response is indeed very similar across all inflation steps. Furthermore, longitudinal stretches are always larger, consistent with the orientation of Langer's lines, which are representative of the collagen orientation.<sup>33,57</sup> The fact that the average deformation is close to unity questions the choice of the grid size since we are unable to determine how far beyond the grid the skin is being deformed.

The total elastic deformation  $F^e$  follows upon excision of the entire expanded patches. We observe a significant difference between the spherical and crescent expanders upon excision: Patch R corresponding to the crescent expander retracts 1.27 in area with an almost isotropic distribution of strain in the two directions of interest; patch P also retracts almost isotropically, but the total area change of 1.42 is significantly larger. The variation between spherical and crescent expanders seems to correlate with the amount of *in vivo* deformation  $F$ . In our initial experiment, the retraction of 1.20 was slightly smaller. One major difference between both inflation protocols is the duration of the expansion process. In the first experiment, we harvested the patches at  $t = 37$  days and the rate of inflation was lower compared to the present protocol. In both experiments, it is impossible to determine whether the tissues have reached a steady state in the adaptation process at the time of tissue harvest. This remains one critical question in our research agenda.

In addition to the elastic patch kinematics, we also quantified the incompatibility. It has been hypothesized that tissue growth increases the effect of residual deformation.<sup>39</sup> By subdividing the excised patches we confirm this hypothesis. The composition of mappings  $F^e \cdot F^{es}$  is the total elastic deformation, and not just  $F^e$  as we had proposed previously. Including the subdivision step, the total elastic area change is 1.39 for the spherical and 1.32 for the crescent expander. Although the longitudinal stretches are always larger than the transverse ones, for the expansion-induced deformation  $F$ , the opposite happens to the elastic deformation  $F^e \cdot F^{es}$ . This is thought provoking and could point to a difference in the growth rates along and perpendicular to the collagen fibers. The contour plots of the elastic deformation depict clearly the discontinuity of the deformation across the smaller patches. Once again,

we highlight the importance of carefully considering the residual deformations induced by growth, which enter our theoretical framework through the intermediate, incompatible configuration. The contours of  $\vartheta^e \cdot \vartheta^{es}$  and  $\lambda_1^e \cdot \lambda_1^{es}$  closely resemble the placement of the expander. The contours of  $\lambda_2^e \cdot \lambda_2^{es}$  are more homogeneous. While it is not a surprise that residual stresses develop in response to growth, this well-known consequence of tissue adaptation has not been thoroughly quantified. The most common approach to determine residual strains in soft tissues is the opening angle experiment, which is specific to arteries or other tubular tissues. In contrast to the method proposed here, it provides only a single global measure of growth. The present study extends the methodology of the opening angle experiment to characterize the regionally varying incompatibility over an entire tissue patch.

The final goal of our analysis is to determine the amount of skin growth attributed to the expansion process. As expected, we confirm that both spherical and crescent expanders result in a net tissue gain.<sup>12</sup> It has been hypothesized that chronic hyper-stretch is the driver of new skin growth.<sup>60</sup> Our results support this hypothesis. All external parameters are the same for both expanders. The difference between both expansion protocols is the amount of expansion-induced deformation  $F$ . The spherical expander induces larger deformations and results in an average area growth of 1.17. The area gain for the crescent expander was 1.10. The contour plots support the hypothesis of hyper-stretch driven growth and are in agreement with our previous finite element predictions<sup>15</sup>: Regions where the expander was placed display a larger amount of growth; regions in the periphery display smaller growth. The difference in the deformation fields imposed by the spherical and crescent expanders can be understood from the mechanical equilibrium problem of the expander interacting with skin, a highly deformable, nonlinear, and anisotropic membrane. When solving this problem in the three-dimensional setting, estimating stress and strain fields is not straightforward and can even escape intuition. We have previously employed finite element simulations to explore the effects of different expander geometries on the deformation of skin membranes.<sup>71</sup>

A limitation of the current study is that we only consider a single animal. We will expand the study to multiple animals to perform multiple repeats of each expander geometry, to vary the expander orientation with respect to Langer's lines, and to vary its placement in the cranial or caudal regions. Another limitation is the assumption of homogeneous mechanical properties over the tissue patches. While we focus only

the back of the pig, it is still possible that small changes in the skin microstructure from cranial to rostral or dorsal to ventral affect the deformation and growth patterns in response to tissue expansion.

The anisotropy of tissue growth deserves special attention. The end result shows that skin grows more in the longitudinal than in the transverse direction. It seems overly simplified though to attribute this difference solely to the expansion-induced deformation  $F$ . A comparison of the differences in the elastic deformation  $F^e \cdot F^{es}$  suggests that the growth rates along and perpendicular to the fiber orientation may be different. A biological explanation of such difference is not possible with our current data and motivates further experiments. We have successfully prototyped investigations to characterize the degree of collagen reorientation induced by growth. Figure 12 left shows a section of the dermis sampled from the control patch. The slice was taken on a plane perpendicular to the skin surface and the tissue was stained with picrosirius red for collagen visualization. The control patch shows the characteristic basket-weave arrangement thick fiber bundles.<sup>47</sup> Figure 12 right, corresponds to a sample from an expanded patch. Collagen fiber bundles are thinner and more disorganized. Since the mechanical properties of skin are influenced primarily by the collagen microstructure in the dermis,<sup>17</sup> quantifying collagen remodeling for regions subjected to different stretches and at different time points during tissue expansion remains a key open question.

Tissue expansion was introduced half a century ago and has since revolutionized the field of plastic and reconstructive surgery.<sup>45</sup> Even 50 years later, there is still no reliable, quantitative preoperative planning tool<sup>8,59</sup>; treatment planning is done on a case by case basis and puts an unnecessary burden on the surgeon's experience and training.<sup>24,38</sup> Even with careful planning, treatment is not free of suboptimal outcomes and complications.<sup>37</sup> One of the many important choices is the selection of an appropriate expander geometry.<sup>46</sup> This decision is difficult to rationalize without a fundamental understanding of the basic mechanisms of skin adaptation to mechanical stimuli.<sup>20</sup> One key element to advance predictive medicine—and tissue expansion in particular—is to synthesize clinical experience and basic sciences into a theoretical model to predict treatment outcomes within a personalized scenario.<sup>69</sup> Our group and others have previously proposed a theoretical and computational model for skin expansion based on the theory of finite growth and finite element analysis.<sup>15,50,61</sup> To demonstrate its clinic potential, we have now established a novel experimental protocol towards a detailed kinematic characterization of skin deformation, prestrain, and growth

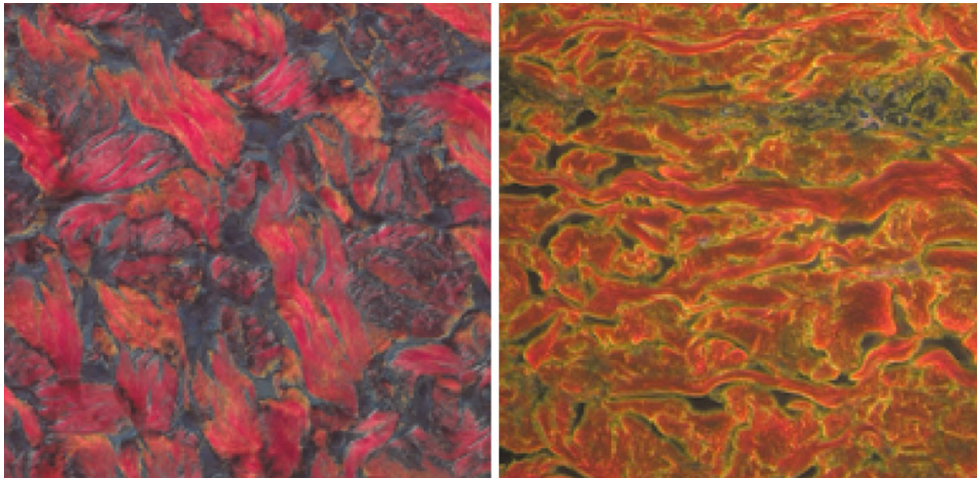


**FIGURE 12.** Collagen remodeling due to tissue expansion and growth. Slices from control and expanded patches are stained with picrosirius red for collagen visualization. The slices correspond to planes perpendicular to the skin surface. In normal, healthy skin, the collagen network exhibits a basket-weave pattern (left). Expansion of skin beyond the physiological regime temporarily alters the collagen network: fiber bundles become thinner and more disorganized (right).

in a chronic porcine model that closely resembles the clinical scenario.<sup>10</sup> We believe that our results constitute a major step towards validating skin expansion models. We hope to continue this work and inspire similar efforts to advance predictive medicine in procedures in which mechanics play a central role .

#### ACKNOWLEDGMENTS

This work was supported by the CONACyT Fellowship, the Stanford Graduate Fellowship, and the DARE Doctoral Fellowship to Adrian Buganza Tepole and by the National Science Foundation CAREER award CMMI 0952021, by the National Science Foundation INSPIRE Grant 1233054, and by the National Institutes of Health Grant U01 HL119578 to Ellen Kuhl.

#### REFERENCES

- <sup>1</sup>Ambrosi, D., G. A. Ateshian, E. M. Arruda, S. C. Cowin, J. Dumais, A. Goriely, G. A. Holzapfel, J. D. Humphrey, R. Kemkemer, E. Kuhl, J. E. Olberding, L. A. Taber, and K. Garikipati. Perspectives on biological growth and remodeling. *J. Mech. Phys. Solids* 59:863–883, 2011.
- <sup>2</sup>Amini, R., C. E. Eckert, K. Koomalsingh, J. McGarvey, M. Minakawa, J. H. Gorman, R. C. Gorman, and M. S. Sacks. On the in vivo deformation of the mitral valve anterior leaflet: effects of annular geometry and referential configuration. *Ann. Biomed. Eng.* 40:1455–1467, 2012.
- <sup>3</sup>Autodesk 123D Catch. Autodesk, Inc. <http://www.123dapp.com/catch>, 2014.
- <sup>4</sup>Bao, G., Y. Bazilevs, J. H. Chung, P. Decuzzi, H. D. Espinosa, M. Ferrari, H. Gao, S. S. Hossain, T. J. R. Hughes, R. D. Kamm, W. K. Liu, A. Marsden, and B. Schrefler. USNCTAM perspectives on mechanics in medicine. *J. R. Soc. Interface* 11(97):20140301, 2014.
- <sup>5</sup>Bartell, T. H., and T. A. Mustoe. Animal models of human tissue expansion. *Plast. Reconstr. Surg.* 83:681–686, 1989.
- <sup>6</sup>Beauchene, J. G., M. M. Chambers, A. E. Peterson, and P. G. Scott. Biochemical, biomechanical, and physical changes in the skin in an experimental animal model of therapeutic tissue expansion. *J. Surg. Res.* 47(6):507–514, 1989.
- <sup>7</sup>Belkoff, S. M., E. C. Naylor, R. Walshaw, E. Lanigan, L. Colony, and R. C. Haut. Effects of subcutaneous expansion on the mechanical properties of porcine skin. *J. Surg. Res.* 58(2):117–123, 1995.
- <sup>8</sup>Bhandari, P. S. Mathematical calculations in a spherical tissue expander. *Ann. Plast. Surg.* 62(2):200–204, 2009.
- <sup>9</sup>Brobmann, F., and J. Huber. Effects of different-shaped tissue expanders on transluminal pressure, oxygen tension, histopathologic changes, and skin expansion in pigs. *Plast. Reconstr. Surg.* 76(5):731–736, 1985.
- <sup>10</sup>Buganza Tepole, A., M. Gart, A. K. Gosain, and E. Kuhl. Characterization of living skin using multi view stereo and isogeometric analysis. *Acta Biomat.* 10:4822–4831, 2014.
- <sup>11</sup>Buganza Tepole, A., M. Gart, C. A. Purnell, A. K. Gosain, and E. Kuhl. Multi-view stereo analysis reveals anisotropy of prestrain, deformation, and growth in living skin. *Bio-mech. Model. Mechanobiol.* 14(5):1007–1019, 2015.
- <sup>12</sup>Buganza Tepole, A., A. K. Gosain, and E. Kuhl. Stretching skin: the physiological limit and beyond. *Int. J. Nonlinear Mech.* 2012(47):938–949, 2012.
- <sup>13</sup>Buganza Tepole, A., A. K. Gosain, and E. Kuhl. Computational modeling of skin: using stress profiles as predictor for tissue necrosis in reconstructive surgery. *Comput. Struct.* 143:32–39, 2014.
- <sup>14</sup>Buganza Tepole, A., H. Kabaria, K. U. Bletzinger, and E. Kuhl. Isogeometric Kirchhoff-Love shell formulations for biological membranes. *Comput. Methods Appl. Mech. Eng.* 293(15):328–347, 2015.
- <sup>15</sup>Buganza Tepole, A., C. J. Ploch, J. Wong, A. K. Gosain, and E. Kuhl. Growin skin: a computational model for skin

- expansion in reconstructive surgery. *J. Mech. Phys. Solids* 59:2177–2190, 2011.
- <sup>16</sup>Cyganek, B., and J. P. Siebert. An Introduction to 3D Computer Vision Techniques and Algorithms. West Sussex: Wiley, 2009.
- <sup>17</sup>Daly, C. H. Biomechanical properties of dermis. *J. Invest. Dermatol.* 79:17–20, 1982.
- <sup>18</sup>De Filippo, R. E., and A. Atala. Stretch and growth: the molecular and physiologic influences of tissue expansion. *Plast. Reconstr. Surg.* 109:2450–2462, 2002.
- <sup>19</sup>Famaey, N., and J. Vander Sloten. Soft tissue modelling for applications in virtual surgery and surgical robotics. *Comput. Methods Biomech. Biomed. Eng.* 11:351–366, 2008.
- <sup>20</sup>Fu, S., J. Fan, L. Liu, H. Jiao, C. Gan, J. Tian, W. Chen, Z. Yang, and Z. Yin. A uniaxial cell stretcher in vitro model simulating tissue expansion of plastic surgery. *J. Craniofac. Surg.* 24(4):1431–1435, 2013.
- <sup>21</sup>Furukawa, Y., and J. Ponce. Accurate, dense, and robust multi view stereopsis. *IEEE Trans. Pattern Anal.* 32:1362–1376, 2010.
- <sup>22</sup>Genet, M., M. K. Rausch, L. C. Lee, S. Choy, X. Zhao, G. S. Kassab, S. Kozerke, J. M. Guccione, and E. Kuhl. Heterogeneous growth-induced prestrain in the heart. *J. Biomech.* 48(10):2080–2089, 2015.
- <sup>23</sup>Göktepe, S., O. J. Abilez, K. K. Parker, and E. Kuhl. A generic approach towards finite growth with examples of athlete's heart, cardiac dilation, and cardiac wall thickening. *J. Mech. Phys. Solids* 58:1661–1680, 2010.
- <sup>24</sup>Gosain, A. K., T. D. Santoro, D. L. Larson, and R. P. Gingrass. Giant congenital nevi: a 20-year experience and an algorithm for their management. *Plast. Reconstr. Surg.* 108:622–636, 2001.
- <sup>25</sup>Gosain, A. K., C. G. Zochowski, and W. Cortes. Refinements of tissue expansion for pediatric forehead reconstruction: a 13-year experience. *Plast. Reconstr. Surg.* 124(5):1559–1570, 2009.
- <sup>26</sup>Hiep, V., Keriven, P., Labatut, P., and J. P. Pons. Towards high-resolution large-scale multi view stereo. In: IEEE Conference on CVPR, 2009.
- <sup>27</sup>Hughes, T. J. R., J. A. Cottrell, and Y. Bazilevs. Isogeometric analysis: CAD, finite elements, NURBS, exact geometry and mesh refinement. *Comput. Methods Appl. Mech. Eng.* 194:4135–4195, 2005.
- <sup>28</sup>Johnson, P. E., D. A. Kernahan, and B. S. Bauer. Dermal and epidermal response to soft-tissue expansion in the pig. *Plast. Reconstr. Surg.* 81:390–395, 1988.
- <sup>29</sup>Jor, J. W. Y., M. P. Nash, P. M. F. Nielsen, and P. J. Hunter. Estimating material parameters of a structurally based constitutive relation for skin mechanics. *Biomech. Model. Mechanobiol.* 10:767–778, 2010.
- <sup>30</sup>Jor, J. W. Y., M. D. Parker, A. J. Taberner, M. P. Nash, and P. M. F. Nielsen. Computational and experimental characterization of skin mechanics: identifying current challenges and future directions. *Wiley Interdiscip. Rev. Syst. Biol. Med.* 5:539–556, 2013.
- <sup>31</sup>Khalatbari, B., and A. Bakhshaeikia. Ten-year experience in face and neck unit reconstruction using tissue expanders. *Burns* 39(3):522–527, 2013.
- <sup>32</sup>Kuhl, E. Growing matter—a review of growth in living systems. *J. Mech. Behav. Biomed. Mater.* 29:529–543, 2014.
- <sup>33</sup>Langer, K. Zur Anatomie und Physiologie der Haut. I. Über die Spaltbarkeit der Cutis. Sitzungsbericht der mathematisch-naturwissenschaftlichen Classe der Kaiserlichen Academie der Wissenschaften, 1861, Abt. 44.
- <sup>34</sup>Lim, K. H., S. Jeyapalina, H. N. Ho, C. M. Chew, P. C. Y. Chen, C. L. Teo, and B. H. Lim. Non-invasive prediction of skin flap shrinkage: a new concept based on animal experimental evidence. *J. Biomech.* 41:1668–1674, 2008.
- <sup>35</sup>Liu, S. Q., and Y. C. Fung. Relationships between hypertension, hypertrophy, and opening angle of zero-stress state of arteries following aortic constriction. *J. Biomech. Eng.* 111:325–335, 1989.
- <sup>36</sup>LoGiudice, J., and A. K. Gosain. Pediatric tissue expansion: indications and complications. *J. Craniofac. Surg.* 14:866–872, 2003.
- <sup>37</sup>Manders, E. K., M. J. Schenden, J. A. Furrey, P. T. Hetzler, T. S. Davis, and W. P. Graham. Soft-tissue expansion: concepts and complications. *Plast. Reconstr. Surg.* 74:493–507, 1984.
- <sup>38</sup>Marcus, J., D. Horan, and J. Robinson. Tissue expansion: past, present and future. *J. Am. Acad. Dermatol.* 23:813–825, 1990.
- <sup>39</sup>Menzel, A. Modelling of anisotropic growth in biological tissues. *Biomech. Model. Mechanobiol.* 3:147–171, 2005.
- <sup>40</sup>Menzel, A., and E. Kuhl. Frontiers in growth and remodeling. *Mech. Res. Commun.* 42:1–14, 2012.
- <sup>41</sup>Meyer, W., K. Neurand, and B. Radke. Elastic fibre arrangement in the skin of the pig. *Arch. Dermatol. Res.* 270:391–401, 1981.
- <sup>42</sup>Meyer, W., K. Neurand, and B. Radke. Collagen fibre arrangement in the skin of the pig. *J. Anat.* 134:139–148, 1982.
- <sup>43</sup>Montagna, W., and J. S. Yun. The skin of the domestic pig. *J. Invest. Dermatol.* 43:11–21, 1964.
- <sup>44</sup>Morykwas, M. J., M. W. Marks, and L. C. Argenta. Surface area and tissue volume increases with differential expansion. *Ann. Plast. Surg.* 28:311–314, 1992.
- <sup>45</sup>Neumann, C. G. The expansion of an area of skin by progressive distension of a subcutaneous balloon. *Plast. Reconstr. Surg.* 19:124–130, 1957.
- <sup>46</sup>Nikkhah, D., L. Yildirimer, and N. W. Bulstrode. Tissue Expansion. Plastic and Reconstructive Surgery: Approaches and Techniques. Hoboken: Wiley, 2015.
- <sup>47</sup>Osman, O. S., J. L. Selway, P. E. Harikumar, C. J. Stocker, E. T. Wargent, M. A. Cawthorne, S. Jassim, and K. Langlands. A novel method to assess collagen architecture in skin. *BMC Bioinformatics* 14(1):260, 2013.
- <sup>48</sup>Pamplona, D. C., and C. R. Carvalho. Characterization of human skin through skin expansion. *J. Mech. Mater. Struct.* 7:641–655, 2012.
- <sup>49</sup>Pamplona, D. C., and D. E. J. S. Mota. Numerical and experimental analysis of inflating a circular hyperelastic membrane over a rigid and elastic foundation. *Int. J. Mech. Sci.* 65:18–23, 2012.
- <sup>50</sup>Pamplona, D. C., R. Q. Velloso, and H. N. Radwanski. On skin expansion. *J. Mech. Behav. Biomed. Mater.* 29:655–662, 2014.
- <sup>51</sup>Piegl, L., and W. Tiller. Curve and surface constructions using rational B-splines. *Comput. Aided Des.* 19:485–498, 1987.
- <sup>52</sup>Pietramaggiore, G., P. Liu, S. S. Scherer, A. Kaipainen, M. J. Prsa, H. Mayer, J. Newalder, M. Alperovich, S. J. Mentzer, M. A. Konerding, S. Huang, D. E. Ingber, and D. P. Orgill. Tensile forces stimulate vascular remodeling and epidermal cell proliferation in living skin. *Ann. Surg.* 246:896–902, 2007.
- <sup>53</sup>Rausch, M. K., N. Famaey, T. O'Brien Shultz, W. Bothe, D. C. Miller, and E. Kuhl. Mechanics of the mitral valve: a critical review, an in vivo parameter identification, and the

- effect of prestrain. *Biomech. Model. Mechanobiol.* 12:1053–1071, 2013.
- <sup>54</sup>Rausch, M. K., and E. Kuhl. On the effect of prestrain and residual stress in thin biological membranes. *J. Mech. Phys. Solids* 61:1955–1969, 2013.
- <sup>55</sup>Rivera, R., J. LoGiudice, and A. K. Gosain. Tissue expansion in pediatric patients. *Clin. Plast. Surg.* 32:35–44, 2005.
- <sup>56</sup>Rodriguez, E. K., A. Hoger, and A. D. McCulloch. Stress-dependent finite growth in soft elastic tissues. *J. Biomech.* 27:455–467, 1994.
- <sup>57</sup>Rose, E. H., G. A. Ksander, and L. M. Vistnes. Skin tension lines in the domestic pig. *Plast. Reconstr. Surg.* 57:729–732, 1976.
- <sup>58</sup>Seitz, S. M., B. Curless, J. Diebel, D. Scharstein, and R. Szeliski. A comparison and evaluation of multi-view stereo reconstruction algorithms. *IEEE Conf. CVPR.* 1:519–528, 2006.
- <sup>59</sup>Shively, R. E. Skin expander volume estimator. *Plast. Reconstr. Surg.* 77:482–483, 1986.
- <sup>60</sup>Silver, F. H., L. M. Siperko, and G. P. Seehra. Mechanobiology of force transduction in dermal tissue. *Skin Res. Technol.* 9:3–23, 2003.
- <sup>61</sup>Socci, L., G. Pennati, F. Gervaso, and P. Vena. An axisymmetric computational model of skin expansion and growth. *Biomech. Model. Mechanobiol.* 6:177–188, 2007.
- <sup>62</sup>Taber, L. Biomechanics of growth, remodeling, and morphogenesis. *Appl. Mech. Rev.* 48:487–545, 1995.
- <sup>63</sup>Tonge, T. K., L. S. Atlan, L. M. Voo, and T. D. Nguyen. Full-field bulge test for planar anisotropic tissues: Part I: Experimental methods applied to human skin tissue. *Acta Biomater.* 9(4):5913–5925, 2013.
- <sup>64</sup>Tong, P., and Y. C. Fung. The stress-strain relationship for the skin. *J. Biomech.* 9:649–657, 1976.
- <sup>65</sup>van Rappard, J. H. A., J. Molenaar, K. van Doorn, G. J. Sonneveld, and J. M. H. M. Borghouts. Surface-area increase in tissue expansion. *Plast. Reconstr. Surg.* 82:833–839, 1988.
- <sup>66</sup>Wang, J. H. C., B. P. Thampatty, J. S. Lin, and H. J. Im. Mechanoregulation of gene expression in fibroblasts. *Gene* 391:1–15, 2007.
- <sup>67</sup>Wong, V. W., K. Levi, S. Akaishi, G. Schultz, and R. H. Dauskardt. Scar zones: region-specific differences in skin tension may determine incisional scar formation. *Plast. Reconstr. Surg.* 129:1272–1276, 2012.
- <sup>68</sup>Zeng, Y. J., Y. H. Liu, C. Q. Xu, X. H. Xu, H. Xu, and G. C. Sun. Biomechanical properties of skin in vitro for different expansion methods. *Clin. Biomech.* 19:853–857, 2004.
- <sup>69</sup>Zöllner, A. M., A. Buganza Tepole, A. K. Gosain, and E. Kuhl. Growing skin—tissue expansion in pediatric forehead reconstruction. *Biomech. Model. Mechanobiol.* 11:855–867, 2012.
- <sup>70</sup>Zöllner, A. M., A. Buganza Tepole, and E. Kuhl. On the biomechanics and mechanobiology of growing skin. *J. Theor. Biol.* 297:166–175, 2012.
- <sup>71</sup>Zöllner, A. M., M. A. Holland, K. S. Honda, A. K. Gosain, and E. Kuhl. Growth on demand—reviewing the mechanobiology of stretched skin. *J. Mech. Behav. Biomed. Mater.* 28:495–509, 2013.